Research Article

Photocatalytic treatment of tannery wastewater using reduced graphene oxide and CdS/ZnO to produce hydrogen with simultaneous sulfide abatement

Elisson A. Souza[1] · Rodrigo J. Araújo[1] · Marcus V. S. Silva[2] · Luciana A. Silva[1,3]

Abstract

This paper addresses the photocatalytic treatment of sulfide-rich liming bath wastewater from tanneries in an oxygen-free atmosphere. The photoactivity assessment of composites obtained from cadmium sulfide (CdS) and zinc oxide (ZnO) hybridization as well the influence of reduced graphene oxide (RGO) on the photocatalytic activity to generate hydrogen and mitigate sulfide was performed under visible-light irradiation. The results of the X-ray diffraction analysis allowed us to identify the crystalline phases in each synthesized sample. The photocatalysts RGO/$(CdS)_{1.0}$/$(ZnO)_{0.4}$ and RGO/$(CdS)_{1.0}$/$(ZnO)_{0.73}$/$(ZnS)_{0.57}$ showed the best performances for hydrogen production of 1.6 mmol g_{cat}^{-1} h^{-1} and 1.4 mmol g_{cat}^{-1} h^{-1}, respectively, with mitigation of 80–90% of the sulfide content in the tannery wastewater. Long-term reaction tests indicated that the photocatalysts are active for a period of 24 h, and they retain the photoactivity after three photocatalytic cycles. The materials have demonstrated great potential for application in energy recovery from tannery wastewater with simultaneous sulfide abatement, especially the photocatalyst RGO/$(CdS)_{1.0}$/$(ZnO)_{0.73}$/$(ZnS)_{0.57}$, which is more eco-friendly because of its lower cadmium content and minimal leaching of this toxic metal ion during photocatalytic treatment.

Keywords Hydrogen · Photocatalysis · Energy recovery · Tannery sludge · Reduced graphene oxide

Mathematics Subject Classification 80A50

1 Introduction

Hazardous tannery effluents are responsible for many negative environmental impacts. They can be divided into three types based on the operations carried out in the different sections [1]. One is the liming bath wastewater that accounts for 45% of the effluent volume and contributes to 30% of the overall biological oxygen demand (BOD) and chemical oxygen demand (COD). The other two types are tanning wastewater with high salinity and high chrome levels and retanning, dyeing, and fat liquoring wastewater that accounts for ~ 20% of the total COD [1].

The liming bath treatment eliminates components from skins that are not transformed into leather [1, 2]. This operation involves treatment using lime and sodium sulfide as the primary chemicals to dissolve hair and destroy the epidermis by breaking the cysteine-disulfide bridges (keratolysis) via reductive division [3]. This type of wastewater is highly alkaline (pH 10–12), with a high sodium sulfide content that is responsible for H_2S evolution [4], which is fatal even in concentrations as low as 200 ppm [5, 6].

The removal of pollutants from liquid effluents is currently considered a major challenge. Several strategies are employed to remove pollutants from wastewater depending on their nature. Adsorption processes using porous

✉ Luciana A. Silva, las@ufba.br | [1]Instituto de Química, Universidade Federal da Bahia, Campus de Ondina, Salvador, BA 40170-155, Brazil. [2]Instituto de Física, Universidade Federal da Bahia, Campus de Ondina, Salvador, BA 40170-155, Brazil. [3]Centro Interdisciplinar de Energia e Ambiente - CIEnAm, Universidade Federal da Bahia, Salvador, BA 40170-290, Brazil.

SN Applied Sciences (2019) 1:1390 | https://doi.org/10.1007/s42452-019-1376-5

Received: 18 July 2019 / Accepted: 27 September 2019 / Published online: 12 October 2019

materials with various functional groups for target ion separation have demonstrated high efficiency for toxic ion removal from water solutions [7–19], whereas degradation processes are mostly employed in remediation of a large number of organic and inorganic pollutants [20–26]. Thus, the use of new environmentally friendly technologies is necessary to mitigate the effects caused by hazardous tannery effluents. Chemical coagulation, electrocoagulation, flocculation, membrane filtration (MF) and advanced oxidation processes (AOPs) are the main solutions proposed and used in the treatment of tannery wastewater [2, 26–28].

Photocatalysis is one type of AOP considered a green technique that offers the potential for complete elimination of toxic chemicals in the environment through its efficiency and broad applicability, and sunlight can be used as an energy source. On the other hand, this process has been applied for solar energy photoconversion to hydrogen and hydrocarbons [29]. Many works [30–34] have shown that the photocatalytic treatment of organic and inorganic species, such as alcohols and sulfide ions, in an oxygen-free atmosphere occurs with simultaneous hydrogen evolution over irradiated semiconductor photocatalyst suspensions. In this context, we recently demonstrated the feasibility of hydrogen generation through photocatalytic treatment of tannery sludge, rich in sulfide ions, using solar power [34]. The process is based on light-driven water splitting in the presence of a sacrificial reactant. Sulfide ions in aqueous solutions act as efficient hole scavengers when metal sulfide-based photocatalysts are employed at high pH [33]. In our previous work [34], the photocatalytic treatment of liming bath wastewater using CdS as a photocatalyst reached a maximum hydrogen production of 294.38 μmol g^{-1} cat h^{-1} at pH 13. Despite the high photocatalytic activity under visible light, which accounts for 43% of sunlight, pure CdS, a narrow bandgap semiconductor (Eg = 2.41 eV), can leach during the photoreaction, increasing the cadmium content in the treated effluent [35], which is a major drawback.

Although TiO_2 is the most commonly used photocatalyst for the degradation of tannery wastewaters with UV irradiation [21–23], in recent years, ZnO has gained more attention due to its ease of crystallization, nontoxicity, high charge mobility and simplicity in morphology adaptation [36], in addition to its high performance in the photocatalytic removal of environmental pollutants [24, 25]. ZnO is a wide bandgap semiconductor (Eg = 3.37 eV), which limits its application as an efficient photocatalyst under sunlight irradiation. Additionally, photogenerated charge carriers have a short lifetime. However, its hybridization with CdS in a CdS/ZnO heterostructure can extend the sensitivity of the composite toward the visible-light region and promote effective charge separation through a type II heterojunction [37, 38]. Due to these properties, the CdS/ZnO heterostructure has been successfully used in photoconversion applications [36, 39–42]. In the present work, we prepared $(CdS)_x/(ZnO)_y$ composites for hydrogen production from liming bath wastewater rich in sulfide ions that act as sacrificial reactants to improve the photocatalytic activity with solar power.

In general, platinum is used as a cocatalyst for hydrogen reduction. When attached on a photocatalyst, platinum nanoparticles can form a Schottky junction, building a barrier that prevents charge recombination [43–45]. In our previous work, an experimental design was performed to evaluate the influence of the platinum precursor ($H_2[PtCl_6]\cdot 6H_2O$) concentration on the photocatalytic hydrogen production from liming wastewater. We concluded that the precursor concentration was not a significant factor due to the deposition of $Pt^{II}S$ on the CdS surface instead of Pt(0) during irradiation, which was confirmed by X-ray analysis [34]. Recently, we evaluated the role of graphene oxide (GO) in a hybrid photocatalyst with CdS for hydrogen production using sulfide ions as sacrificial reactants [46]. Our findings demonstrated that reduced graphene oxide (RGO), which is produced during the photoreaction, acts as an efficient electron trap. The trapped electrons can be transferred to adsorbed water molecules on the surface that promote the reduction in water to H_2, and the photogenerated holes can oxidize sulfide ions to polysulfides and sulfate on the CdS surface. In the present work, we evaluated the photoactivity of $RGO/(CdS)_x/(ZnO)_y$ as bifunctional photocatalysts in the treatment of liming bath wastewater to mitigate pollutants with simultaneous hydrogen production.

2 Experimental details

2.1 Materials and chemicals

The chemicals used in the synthesis, photocatalytic tests and wastewater analyses were of analytical grade, and all of them were used as purchased. Graphite, potassium permanganate, sodium sulfide nonahydrate, ethylene glycol and 30% hydrogen peroxide solution were purchased from Sigma-Aldrich. Sulfuric acid was purchased from Qhemis, while citric acid, cadmium chloride monohydrate and zinc nitrate hexahydrate were purchased from Merck.

2.2 Photocatalyst preparation

The binary composites $(CdS)_x/(ZnO)_y$ were prepared by the Pechini method, followed by sulfurization via ion exchange in a sodium sulfide solution. The precursors used here were $CdCl_2\cdot H_2O$ and $Zn(NO_3)_2\cdot 6H_2O$ with molar

ratios $y/x = 0$, 0.2, 0.4, 0.6, 1.5 and 4.0. Briefly, the procedure consisted of dissolution of an appropriate amount of the precursors in 50 mL of water. This solution was added to an EG/CA solution prepared with 10 mL of ethylene glycol and 7.0 g of citric acid in 50 mL of water. The mixture was kept at 80 °C to obtain the metal-citrate complex; then, the temperature was raised to 120 °C to form a gel, which was polymerized at 300 °C for 4 h and calcined at 500 °C for 4 h. The solids were grounded and suspended in a sodium sulfide solution (0.5 mol L^{-1}) for 12 h to promote ion exchange (IE) and then filtered and dried at 60 °C for 12 h. The samples were labeled Zn/Cd0.0, Zn/Cd0.2, Zn/Cd0.4, Zn/Cd0.6, Zn/Cd1.5 and Zn/Cd4.0 before ion exchange and Zn/Cd0.0-IE, Zn/Cd0.2-IE, Zn/Cd0.4-IE, Zn/Cd0.6-IE, Zn/Cd1.5I-E and Zn/Cd4.0-IE after ion exchange.

The ternary composites RGO/$(CdS)_x$/$(ZnO)_y$ were prepared by mechanical mixing of binary composites $(CdS)_x$/$(ZnO)_y$ with graphite oxide (2% w/w) obtained by the Hummers' method [47, 48]. The mixture was placed in a photoreactor with an appropriate amount of tannery wastewater and exposed to high-intensity ultrasound irradiation using an ultrasonic wave source (R2D091109, Unique) under ambient air for 15 min with the power adjusted at 80 W to promote the exfoliation of graphite oxide to produced graphene oxide (GO). The photoreduction of GO to RGO occurred in situ during hydrogen generation.

2.3 Photocatalyst characterization

The synthesized materials were analyzed as powders by XRD (Shimadzu XRD6000) using CuKα, Ni-filtered radiation, and a scanning rate of 2° 2θ min^{-1} in a 2θ range of 5°–80°, at 35 kV and 15 mA. The chemical composition of the samples was determined by energy-dispersive X-ray fluorescence (Shimadzu EDX720). UV–Vis diffuse reflectance spectra were recorded on a Thermo Scientific Evolution 600 UV–Vis spectrometer using a praying mantis accessory. Selected samples were analyzed before and after irradiation by Raman spectroscopy using a dispersive Raman spectrometer, Jasco NRS-5100, with 0.4 cm^{-1} resolution. SEM images were taken by a JSM-6610LV scanning electron microscope (JEOL) operated at 20 kV after gold metallization.

2.4 Sacrificial reactant

The target effluent used as a sacrificial reactant was collected from a tannery located in Petrolina-PE, Brazil. All details about the effluent are described elsewhere [34]. To prepare the aqueous solutions used in the photocatalytic tests, first, the wastewater as collected was centrifuged to remove the solid materials and then diluted to 50% V/V with distilled water. Total sulfide, before and after irradiation, was also determined by the iodometric method of analysis using sodium thiosulfate, following the procedure described in [49]. Sulfate was quantified by a standard gravimetric method with precipitation as $BaSO_4$ in the presence of HCl by the addition of $BaCl_2$. Biological demand of oxygen (BDO) and chemical demand of oxygen (CDO) were determined by Standard Methods for the Examination of Water and Wastewater 5210 B and 5220 A/C, respectively. Cadmium was quantified using a FAAS Agilent Technologies 200 Series AA—Model 240FS AA and an analytical curve in the concentration range of 0.5–2.5 mg L^{-1}.

2.5 Photocatalytic reactions

For each photocatalytic test, 60 mg of a given binary composite was mechanically mixed with 1.2 mg of graphite oxide, weighed in a Mettler Toledo microbalance, model MX5, $d = 1$ µg, and dispersed in 60 mL of diluted tannery sludge (50% V/V) with the pH adjusted to 13 by the addition of a NaOH solution. The mixture was sonicated for 15 min to promote graphite oxide exfoliation. Then, the photocatalytic cell was purged with argon for 30 min to eliminate oxygen gas. The collimated light beam from a high-pressure 500 W Hg–Xe arc lamp was passed through an IR filter, and a 420-nm cutoff filter before reaching the flat window of the photocatalytic cell that was maintained at a constant temperature by air cooling. The photocatalytic cell was equipped with argon gas inlet/outlet tubes to collect and transfer gaseous products to the analytical system. Hydrogen gas evolution was measured by gas chromatography (SHIMADZU, GC2014) with a thermal conductivity detector (TCD) and argon as the carrier gas. Aliquots of 1 mL of the gas phase were injected in the GC system in intervals of 1 h. To quantify the hydrogen produced during the reaction, a 5% H_2 standard diluted in argon was injected before each experiment. For comparison, all tests were also performed without GO as well as with CdS obtained by the thermal method [33]. The experiments were performed in triplicate.

3 Results and discussion

The XRD patterns for the samples prepared by the Pechini method before (Zn/Cd0.0, Zn/Cd0.2, Zn/Cd0.4, Zn/Cd0.6, Zn/Cd1.5 and Zn/Cd4.0) and after (Zn/Cd0.0-IE, Zn/Cd0.2-IE, Zn/Cd0.4-IE, Zn/Cd0.6-IE, Zn/Cd1.5-IE and Zn/Cd4.0-IE) ion exchange are shown in Fig. 1. In general, samples before the ion exchange process are crystalline. ZnO and $CdCl_2{\cdot}H_2O$ were the predominant phases, except for sample Zn/Cd0.0 (no zinc), for which the XRD pattern showed low crystallinity and $CdCl_2{\cdot}H_2O$ as a single phase (Fig. 1a).

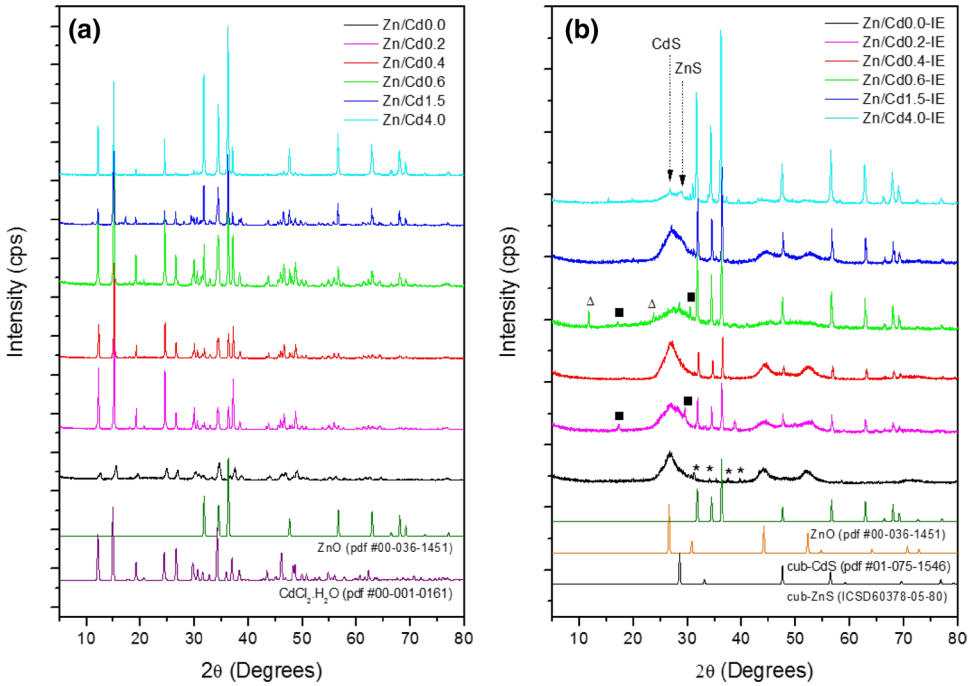

Fig. 1 XRD patterns for the samples before (**a**) and after (**b**) ion exchange: (filled square) CdOHCl (pdf #01-074-1047), (open triangle) lamellar compound not identified and (asterisks) $Cd_3Cl_2O_2$ (pdf #01-084-2209)

After ion exchange (Fig. 1b), the $CdCl_2{\cdot}H_2O$ in sample Zn/Cd0.0 was virtually converted into CdS, with a cadmium residue as $Cd_3Cl_2O_2$. For samples Zn/Cd0.2-IE, Zn/Cd0.4-IE and Zn/Cd0.6-IE, the ZnO phase was preserved and $CdCl_2{\cdot}H_2O$ disappeared to give rise to the CdS cubic phase with residues of the CdOHCl phase and a lamellar compound not identified in samples Zn/Cd0.2-IE and Zn/Cd0.6-IE. For samples Zn/Cd1.5-IE and Zn/Cd4.0-IE, the ZnS cubic phase was identified.

The EDX analysis provided the zinc, cadmium and sulfur contents used to calculate the y/x experimental ratio in the general formula $(CdS)_x/(ZnO)_y$ and nCd/nS experimental molar ratio (Table 1). The experimental values of y/x are larger than the nominal values, suggesting that cadmium is lixiviated during the ion exchange process, except for sample Zn/Cd0.4-IE, where the experimental and nominal values are the same. On the other hand, the nCd/nS molar ratio gives the ion exchange index to form CdS. Samples Zn/Cd0.0-IE and Zn/Cd0.4-IE have values of approximately 1, which means that all cadmium is virtually converted into CdS. The ratios for samples Zn/Cd0.2-IE and Zn/Cd0.6-IE are larger than 1.0, indicating that cadmium is not completely present as CdS, which is in accordance with the XRD analysis that identified CdOHCl as a segregated phase in both samples. Samples Zn/Cd1.5-IE and Zn/Cd4.0-IE, with low cadmium contents, have an ion exchange index less than 1.0 due to zinc sulfide formation, as identified in the XRD patterns of these samples (Fig. 1b).

The diffuse reflectance spectra of the samples after ion exchange show two absorption structures related to CdS and ZnO (Fig. 2). The ZnO-related absorption at approximately 400 nm increases due to the increasing content of Zn in the composites. The absorption edges for all samples are compatible with the CdS spectrum, but the presence of cadmium compound segregated phases and ZnS results in a blueshift. According to the UV–Vis spectra, one can classify the samples into three groups: (i) samples without segregated phases of cadmium compounds, Zn/Cd0.0-IE and Zn/Cd0.4-IE; (ii) samples with segregated phases of

Table 1 EDX elemental analysis (% wt/wt), *y*/*x* ratio for the general formula $(CdS)_x/(ZnO)_y$ and nCd/nS ratio (mol/mol) obtained from EDX results

Sample	Elemental analysis (% wt/wt)			*y*/*x* (mol/mol)		nCd/nS (mol/mol)
	Cd	Zn	S	Nominal	Experimental	
Zn/Cd0.0-IE	78.1	21.9	0.0	0	0	1.01
Zn/Cd0.2-IE	55.9	12.5	16.0	0.2	0.5	1.27
Zn/Cd0.4-IE	60.1	18.3	14.9	0.4	0.4	0.94
Zn/Cd0.6-IE	51.51	10.8	21.4	0.6	0.7	1.36
Zn/Cd1.5-IE	41.7	16.8	30.7	1.5	1.3	0.43
Zn/Cd4.0-IE	19.7	8.9	56.9	4.0	5.0	0.63

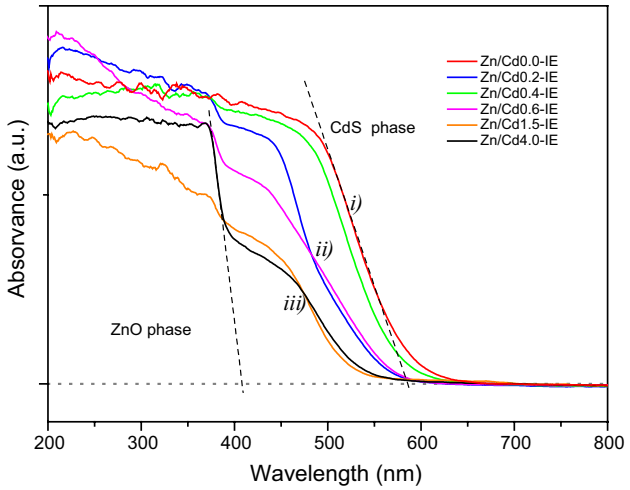

Fig. 2 UV-Vis spectra of the samples after ion exchange: (i) samples without segregated phases of cadmium compounds, (ii) samples with segregated phases of cadmium compounds, and (iii) samples with ZnS phase

Table 2 The optical bandgap energies of the samples determined by a geometrical method

Sample	Eg (eV)
Zn/Cd0.0-IE	2.24
Zn/Cd0.2-IE	2.38
Zn/Cd0.4-IE	2.28
Zn/Cd0.6-IE	2.39
Zn/Cd1.5-IE	2.50
Zn/Cd4.0-IE	2.46

cadmium compounds, Zn/Cd0.2-IE and Zn/Cd0.6-IE; and (iii) samples with ZnS phase, Zn/Cd1.5-IE and Zn/Cd4.0-IE.

The bandgap energies were obtained from the UV–Vis spectral data by geometrical method [50]. The values were determined using equation $Ihv = A(hv - \mathrm{Eg})^{1/2}$ considering the direct gap transition, where I is the absorption intensity, A is a coefficient, and hv is the photon energy. The values of Eg were obtained by extrapolation of the best linear fit for $(Ihv)^2$ and hv up to the point where the fit crosses the ordinate axis and are summarized in Table 2.

The bandgap energy values are quite similar for each group. For group i, samples Zn/Cd0.0-IE and Zn/Cd0.4-IE, the bandgap energies are 2.24 eV and 2.28 eV, respectively. For group ii, samples Zn/Cd0.2-IE and Zn/Cd0.6-IE, the bandgap energies are 2.38 eV and 2.39 eV, respectively. However, for these two groups, the experimental bandgap energies are less than those reported in the literature for CdS (Eg = 2.41 eV). Finally, for group iii, samples Zn/Cd1.5-IE and Zn/Cd4.0-IE, the bandgap energies are 2.50 eV and 2.46 eV, respectively, which are greater than that of CdS due to the presence of ZnS (Eg = 3.7 eV) in these composites.

SEM images of the samples after ion exchange (Zn/Cd0.0-IE, Zn/Cd0.2-IE, Zn/Cd0.4-IE, Zn/Cd0.6-IE, Zn/Cd1.5-IE and Zn/Cd4.0-IE) are depicted in Fig. 3. Micrographs show an irregular morphology for all samples, and plaques are predominant in the low zinc content samples and small rods in the high zinc content samples. A spongy aspect is also observed, which suggests the presence of nanoparticles.

All samples after ion exchange were tested as photocatalysts in the treatment of liming bath wastewater in an oxygen-free atmosphere under visible-light irradiation ($\lambda > 420$ nm). Figure 4 shows the hydrogen production profiles for the composites without RGO (a) and with 2% RGO (b) and compares the performance of CdS obtained by the thermal method in the same photocatalytic system. All photocatalysts evaluated were photoactive for hydrogen production under visible-light irradiation. In general, the composites presented better performances than pure CdS (Zn/Cd0.0-IE and CdS obtained by the thermal method), and the presence of RGO contributed to improving the photocatalytic activity. The sample with the best performance was RGO/(Zn/Cd0.4-IE), with a hydrogen production rate of 1.6 mmol g_{cat}^{-1} h^{-1}, which is a fourfold enhancement in the photocatalytic activity compared to RGO/CdS and more than fivefold compared to pure CdS. It is followed by RGO/(Zn/Cd1.5-IE) with a hydrogen production rate of 1.4 mmol g_{cat}^{-1} h^{-1}.

The XRD and EDX elemental analyses have shown that the Zn/Cd0.4-IE sample is the composite $(CdS)_{1.0}/(ZnO)_{0.4}$ (experimental y/x = 0.4) without any other segregated phases, while the Zn/Cd1.5-IE sample has a ZnS phase in addition to CdS and ZnO with a composition of $(CdS)_{1.0}/(ZnO)_{0.73}/(ZnS)_{0.57}$ (experimental $y/x = 1.3$) (Fig. 1 and Table 1). To confirm a heterojunction effect, we performed the same photocatalytic tests with mechanical mixtures of the individual components. The photocatalysts with the best performance, Zn/Cd0.4-IE and Zn/Cd1.5-IE, were selected to prepare mechanical mixtures according to the elemental analysis, called Zn/Cd0.4-MM and Zn/Cd1.5-MM, respectively. Appropriate amounts of ZnO, obtained by the Pechini method, and CdS and/or ZnS, obtained by the precipitation method, and GrO were placed in a photoreactor containing the wastewater. The profile of hydrogen production under visible-light irradiation as a function of time for such photocatalysts as well as a test with pure RGO is shown in Fig. 5.

The amount of hydrogen produced using composites as photocatalysts in both cases is much higher than that obtained from the mechanical mixtures of the individual components, reflecting the heterojunction effect on the composites RGO/$(CdS)_{1.0}/(ZnO)_{0.4}$ (labeled RGO/(Zn/Cd0.4-IE)) and RGO/$(CdS)_{1.0}/(ZnO)_{0.73}/(ZnS)_{0.57}$ (labeled RGO/(Zn/

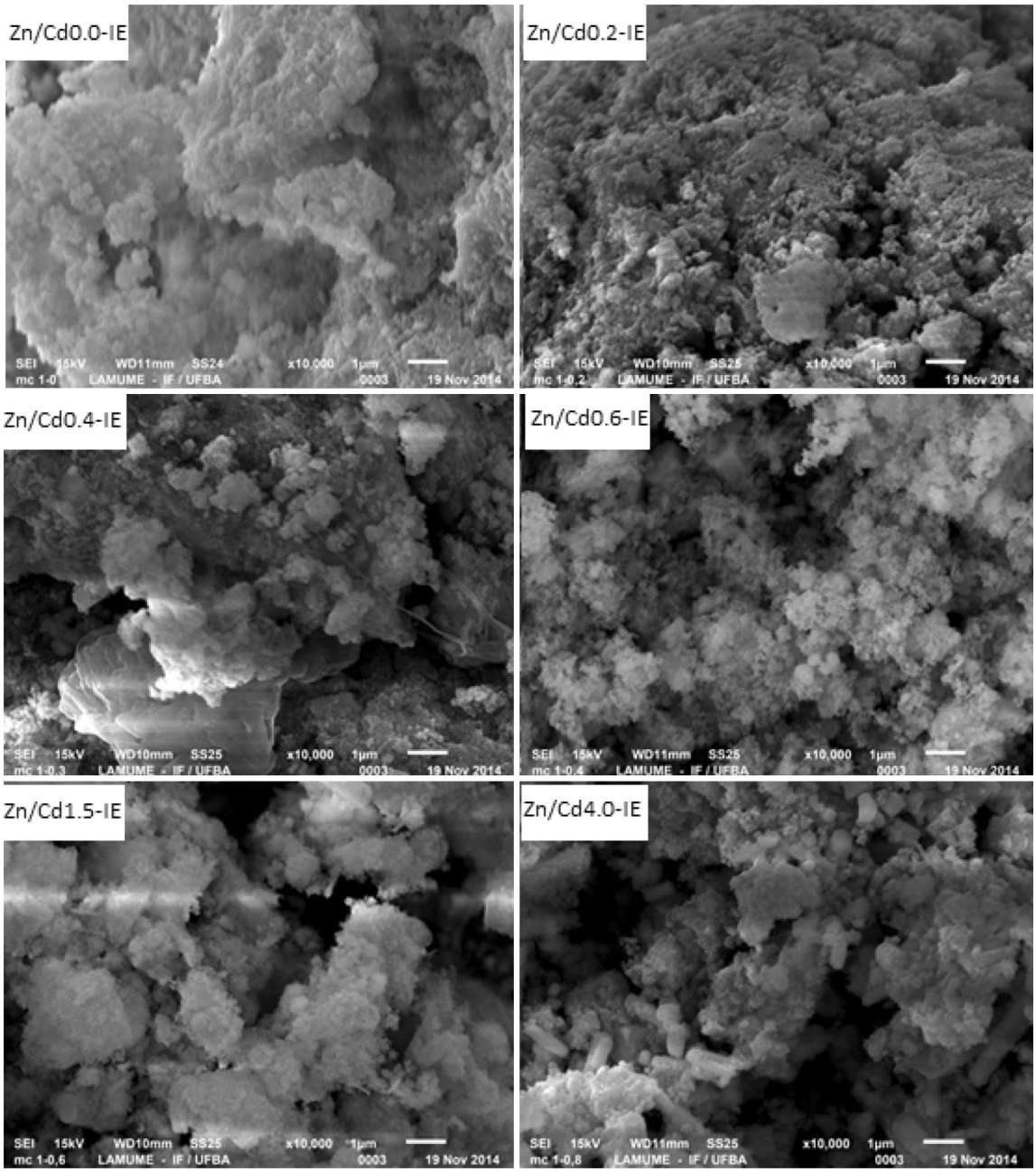

Fig. 3 SEM images of the samples after ion exchange: Zn/Cd0.0-IE, Zn/Cd0.2-IE, Zn/Cd0.4-IE, Zn/Cd0.6-IE, Zn/Cd1.5I-E and Zn/Cd4.0-IE

Cd1.5-IE)) obtained by the Pechini method followed by sulfurization.

All photocatalysts were collected after the photoreaction, washed and dried at room temperature. The powders were analyzed by X-ray diffraction and Raman spectroscopy to identify all components in the composites and mechanical mixtures after irradiation and to prove the reduction in GO to RGO (Fig. 6).

According to the XRD results, there is no significant difference between samples before (Fig. 6a) and after (Fig. 6b) irradiation. However, for sample RGO/(Zn/Cd1.5-IE), additional peaks appeared. Due to the small amount of RGO component (2%) in the composites and mechanical mixtures, we could identify only a small shoulder around 20° (2θ) in the samples RGO/(Zn/Cd0.4-IE) and RGO/(Zn/Cd1.5-IE), indicating a small stacking degree of RGO in the photocatalysts with the best performance.

Raman spectroscopy has been applied extensively to monitor graphitic materials [51]. In this work, it was used to confirm the graphene oxide reduction and to identify the

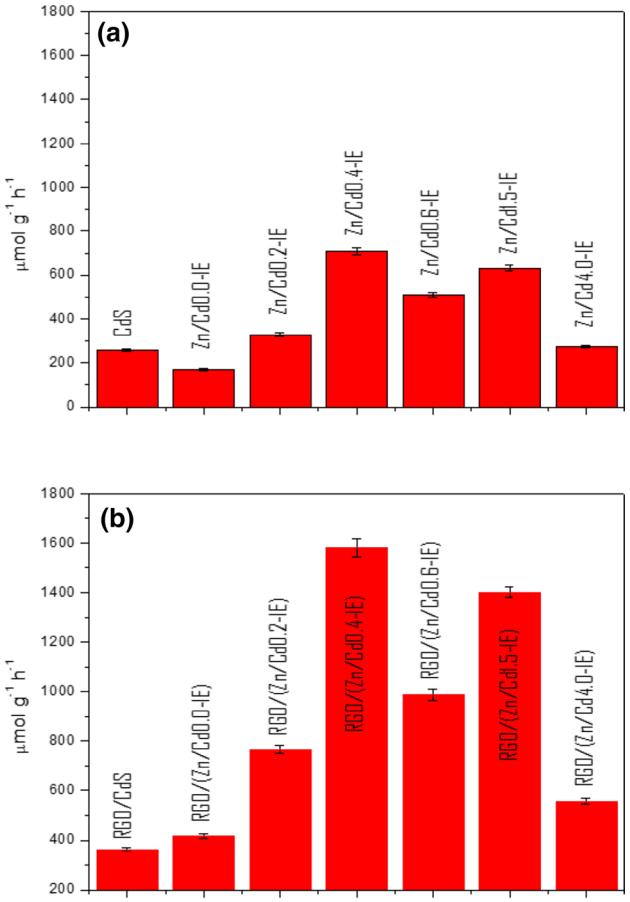

Fig. 4 Hydrogen production rate of different photocatalysts under visible-light irradiation ($\lambda > 420$ nm): **a** photocatalysts without RGO and **b** photocatalysts with RGO

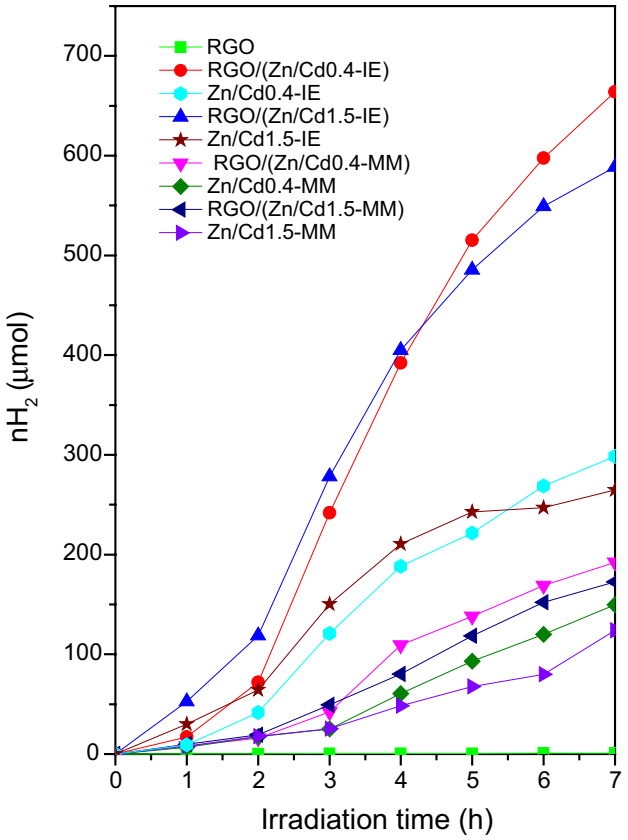

Fig. 5 Hydrogen production as a function of time for different composites and mechanical mixtures as well as pure RGO under visible-light irradiation ($\lambda > 420$ nm)

components in the composites and mechanical mixtures before and after irradiation (Fig. 7). From the comparison among the Raman spectra of individual components (CdS, ZnS and ZnO) (Fig. 8a), composites (Zn/Cd0.4-IE and Zn/Cd1.5-IE) and mechanical mixtures (Zn/Cd0.4-MM and Zn/Cd1.5-MM) (Fig. 8b), one can see peaks related to CdS and ZnO in all evaluated samples. However, for the samples Zn/Cd1.5-IE and Zn/Cd1.5-MM, which contain ZnS as one of the components, the intense peaks of CdS hide the ZnS-related peaks. The peaks related to CdS can be observed at approximately 302 cm^{-1} (LO), 603 cm^{-1} (2-LO) and 899 cm^{-1} (3-LO) [52], all of which are assigned to optical phonon modes (LO, first and second overtones). The first two, which are strong and narrow, imply good crystallinity and an ordered structure [53]. Near the main CdS peak, a small but constant peak located at 348 cm^{-1} (multiphonon process) is also attributed to CdS [54, 55]. Finally, the other peaks located at 420 cm^{-1} (E2 mode) and 578 cm^{-1} (A1-LO mode) are related to the ZnO structure [56].

The behavior of the two well-known prominent peaks related to graphene, the D band and G band, in the Raman measurements (Fig. 7c) confirms the reduction in GO to RGO [57]. In addition to the increasing ratio I_D/I_G compared to the ratio for GO [58], a sp^3/sp^2 ratio reflex, it is possible to observe a small redshift in the G band, from 1599 to 1582 cm^{-1}, especially for the highest performance photocatalysts, RGO/(Zn/Cd0.4-IE) and RGO/(Zn/Cd1.5-IE). This result is indicative of the restoration of the C=C sp^2 bond [59, 60], as found in the graphene hexagonal lattice.

Reduced oxide graphene (RGO) plays an important role in the charge transfer process in photocatalytic reactions since it promotes spatial separation of charges and prevents recombination processes [61–73]. In addition, RGO can transfer electrons to adsorbed water molecules on its surface to produce hydrogen. Thus, a possible mechanism for this process is based on the oxidation of sulfide ions from tannery sludge by photogenerated holes on the ZnO surface, while molecular hydrogen is formed from the reduction in water on the RGO surface. Cadmium sulfide is the component responsible for generating charge carriers upon visible-light absorption. The scheme in Fig. 8 illustrates the proposed generation and charge transfer through the RGO/CdS/ZnO heterojunction.

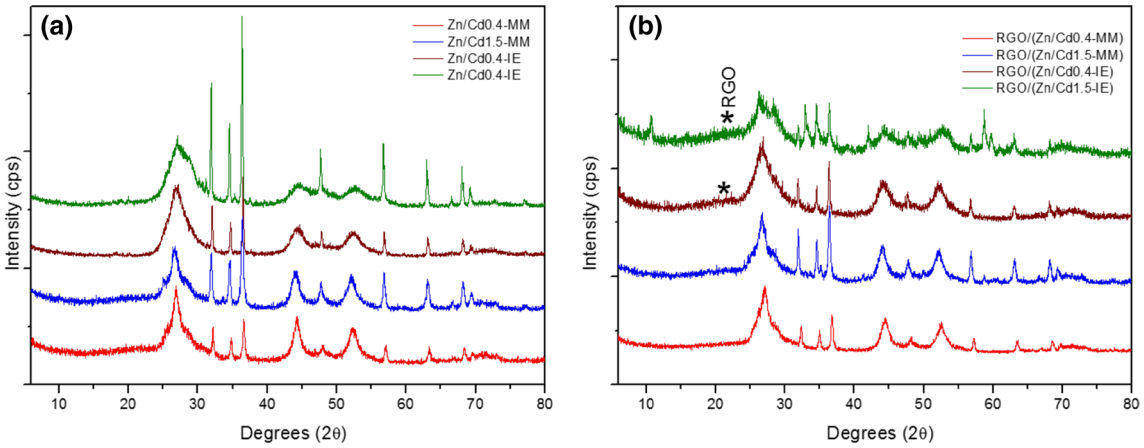

Fig. 6 XRD patterns of the composites and mechanical mixture samples before (**a**) and after (**b**) irradiation

The photocatalyst RGO/$(CdS)_{1.0}$/$(ZnO)_{0.73}$/$(ZnS)_{0.57}$ exhibits slightly lower photocatalytic activity than the photocatalyst RGO/$(CdS)_{1.0}$/$(ZnO)_{0.4}$ for hydrogen production (Figs. 4 and 5), which implies that the presence of a ZnS segregated phase, inactive under visible-light irradiation, decreases the number of visible-light-absorption centers that contribute to the photocatalytic activity.

To evaluate the photocatalyst deactivation and the efficiency of mitigating sulfide and organic matter, a long-term reaction was performed over 30 h for both RGO/$(CdS)_{1.0}$/$(ZnO)_{0.4}$ and RGO/$(CdS)_{1.0}$/$(ZnO)_{0.73}$/$(ZnS)_{0.57}$. The residual liquid phase was analyzed after tannery sludge treatment with each photocatalyst and compared with the wastewater before photocatalytic treatment. The total loss of photocatalytic activity was identified after 24 h of irradiation (Fig. 9), reaching a maximum amount of hydrogen of 1.2 mmol for RGO/$(CdS)_{1.0}$/$(ZnO)_{0.4}$ and 1.0 mmol for RGO/$(CdS)_{1.0}$/$(ZnO)_{0.73}$/$(ZnS)_{0.57}$. The characterization results of the liming bath wastewater before and after photocatalytic treatment are shown in Table 3.

The sulfide content in the liming bath wastewater decreased sharply after photocatalytic treatment from 55.0 g L^{-1} in the untreated wastewater to 5.4 g L^{-1} when treated with RGO/$(CdS)_{1.0}$/$(ZnO)_{0.4}$ and 8.9 g L^{-1} when treated with RGO/$(CdS)_{1.0}$/$(ZnO)_{0.73}$/$(ZnS)_{0.57}$. The sulfide is partially converted into sulfate, and its content increased from 3.8 g L^{-1} in the untreated wastewater to 7.0 g L^{-1} when the photocatalyst used in the treatment was RGO/$(CdS)_{1.0}$/$(ZnO)_{0.4}$ and 6.4 g L^{-1} when the photocatalyst was RGO/$(CdS)_{1.0}$/$(ZnO)_{0.73}$/$(ZnS)_{0.57}$. These photocatalysts play a bifunctional role in the photocatalytic treatment of tannery wastewater in an oxygen-free atmosphere, mitigating 80–90% of the sulfide content with simultaneous hydrogen production. Because the photocatalytic treatment of the tannery sludge was conducted in an oxygen-free atmosphere to recover the energy contained in the waste, much of the organic matter remains in the liquid. Although a decrease in both BOD and COD has been observed, this treatment is not sufficient for total abatement of the organic matter present in the residue.

The characterization of the liming bath wastewater before and after photocatalytic treatment allowed the evaluation of the photocatalyst stability with respect to cadmium leaching (Tabela 3). Despite the slightly higher photocatalytic activity of the photocatalyst RGO/$(CdS)_{1.0}$/$(ZnO)_{0.4}$, the photocatalyst RGO/$(CdS)_{1.0}$/$(ZnO)_{0.73}$/$(ZnS)_{0.57}$ is more eco-friendly because its cadmium content is lower and there is virtually no loss of this metal by leaching during photocatalytic treatment.

To evaluate the reuse of the photocatalysts, three photocatalytic cycles were performed over 24 h using the same photocatalyst, RGO/$(CdS)_{1.0}$/$(ZnO)_{0.4}$ and RGO/$(CdS)_{1.0}$/$(ZnO)_{0.73}$/$(ZnS)_{0.57}$, and fresh tannery sludge for each cycle. In the first photocatalytic cycle, fresh photocatalyst was used, collected after irradiation, washed with deionized water and subsequently used in the second photocatalytic cycle. The procedure was repeated for the third photocatalytic cycle. The results are shown in Fig. 10, noting that the hydrogen production profiles for both photocatalysts are identical for the three cycles.

It is possible to conclude that the photocatalysts do not lose activity for at least three photocatalytic cycles. In this way, the halt in hydrogen production after 24 h of irradiation in the long-term reaction (Fig. 9) must be associated with the consumption of the sacrificial reagent (sulfide) instead of photocatalyst deactivation.

4 Conclusions

The results revealed that this synthesis procedure is capable of obtaining $(CdS)_x$/$(ZnO)_y$ composites and that GO reduction takes place in situ during the photoreaction to

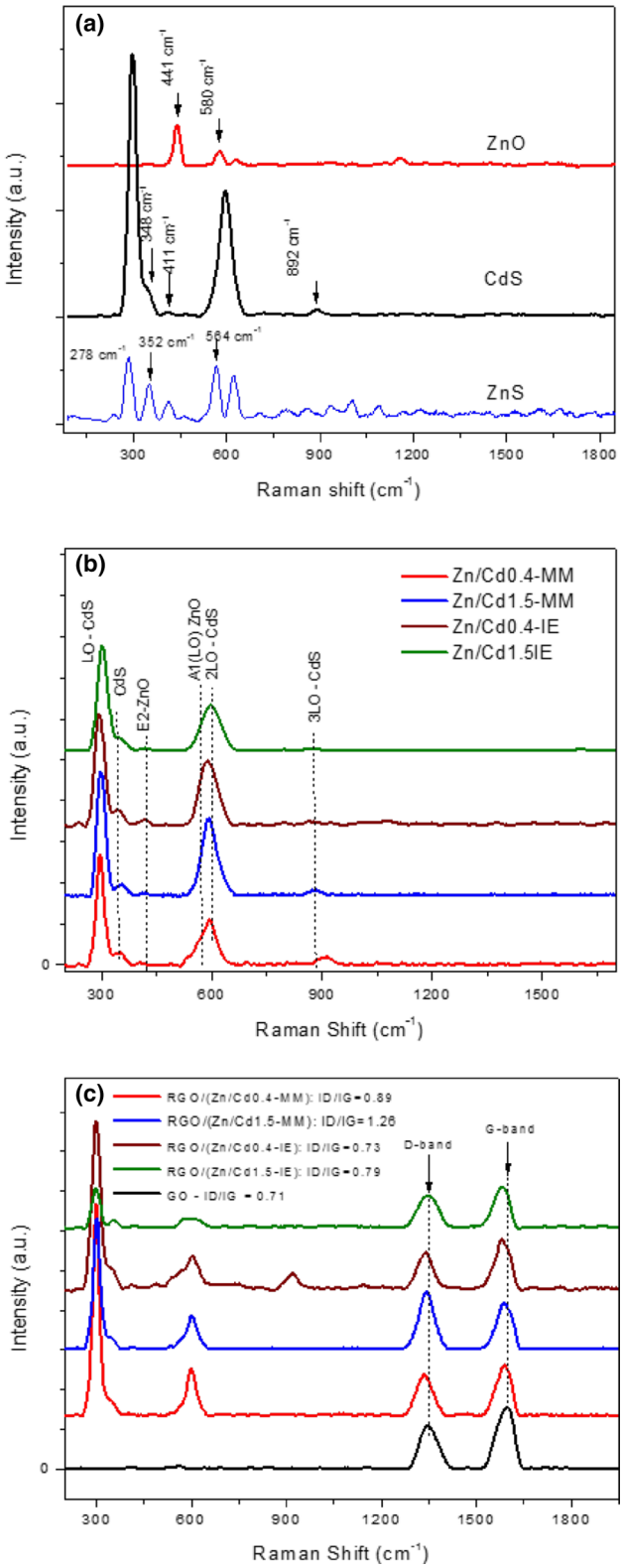

Fig. 7 Raman spectra: **a** individual components (ZnO, CdS and ZnS); **b** composites and mechanical mixtures without GO before irradiation and **c** composites and mechanical mixtures with GO after irradiation

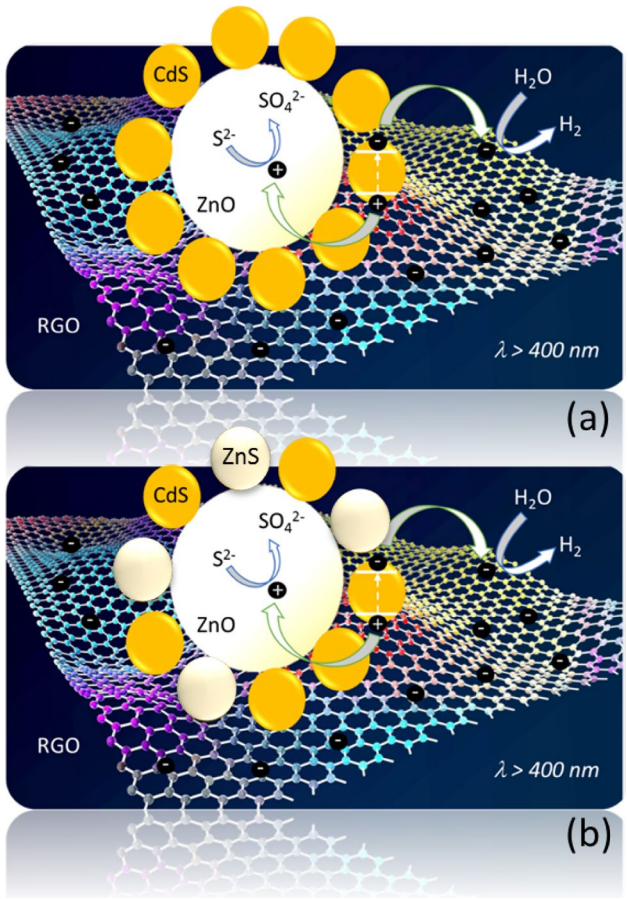

Fig. 8 Primary steps of charge transfer through the RGO/CdS/ZnO heterojunction in the photocatalysts to promote the redox reaction: **a** RGO/$(CdS)_{1.0}$/$(ZnO)_{0.4}$ and **b** RGO/$(CdS)_{1.0}$/$(ZnO)_{0.73}$/$(ZnS)_{0.57}$

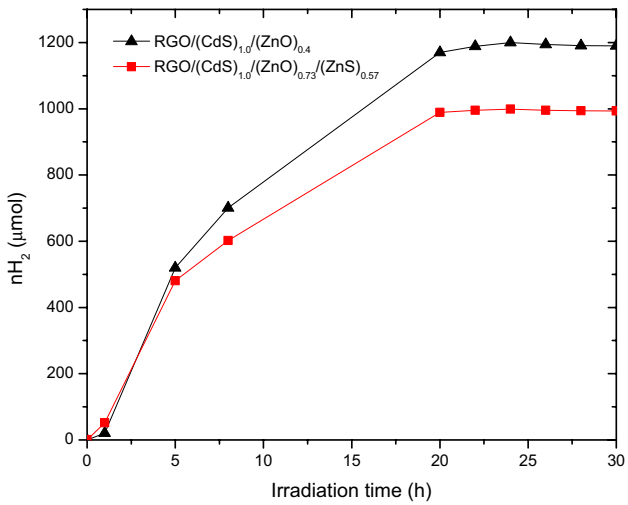

Fig. 9 Hydrogen production profile in a long-term reaction for tannery sludge treatment with the photocatalysts RGO/$(CdS)_{1.0}$/$(ZnO)_{0.4}$ and RGO/$(CdS)_{1.0}$/$(ZnO)_{0.73}$/$(ZnS)_{0.57}$

Table 3 Characterization of the liming bath wastewater before and after photocatalytic treatment with RGO/$(CdS)_{1.0}$/$(ZnO)_{0.4}$ and RGO/$(CdS)_{1.0}$/$(ZnO)_{0.73}$/$(ZnS)_{0.57}$

Liming bath wastewater before photocatalytic treatment	Sulfide $g\ L^{-1}$	Sulfate $g\ L^{-1}$	CDO[a] $g\ L^{-1}$	BDO[b] $g\ L^{-1}$	Cd $mg\ L^{-1}$
	55.0	3.8	4.99	2.14	0.82

Liming bath wastewater after photocatalytic treatment

Photocatalyst	Sulfide $g\ L^{-1}$	Sulfate $g\ L^{-1}$	CDO[a] $g\ L^{-1}$	BDO[b] $g\ L^{-1}$	Cd $mg\ L^{-1}$
$(CdS)_{1.0}/(ZnO)_{0.4}$	5.4	7.0	3.52	1.32	1.20
$(CdS)_{1.0}/(ZnO)_{0.73}/(ZnS)_{0.57}$	8.9	6.4	3.97	1.70	0.88

[a]Chemical demand of oxygen

[b]Biological demand of oxygen

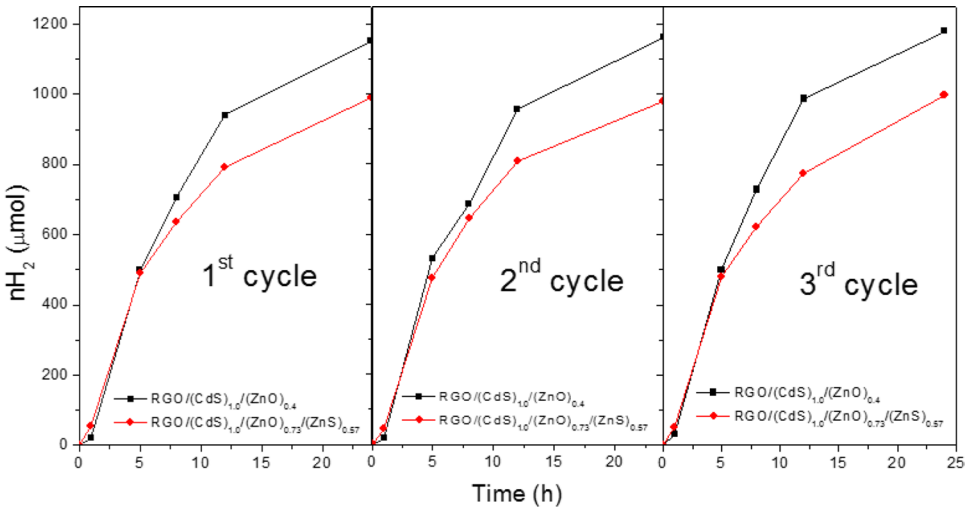

Fig. 10 Recycle tests using the photocatalysts RGO/$(CdS)_{1.0}$/$(ZnO)_{0.4}$ and RGO/$(CdS)_{1.0}$/$(ZnO)_{0.73}$/$(ZnS)_{0.57}$

produce composites such as RGO/$(CdS)_x$/$(ZnO)_y$. Among all photocatalysts tested in this work, the composite named Zn/Cd0.4-IE, with the empirical formula $(CdS)_{1.0}/(ZnO)_{0.4}$, in the presence of RGO was the most active in the treatment of liming bath wastewater from tanneries to produce hydrogen with simultaneous sulfide abatement. The best activity can be associated with the absence of segregated phases and the narrower bandgap energy, covering a large portion of the visible-light range. The presence of ZnS as a segregated phase in sample Zn/Cd1.5-IE, with the empirical formula $(CdS)_{1.0}/(ZnO)_{0.73}/(ZnS)_{0.57}$, resulted in a slight decrease in the photocatalytic activity relative to $(CdS)_{1.0}/(ZnO)_{0.4}$, but this photocatalyst has the advantage of a lower cadmium content and does not suffer from leaching during photocatalytic treatment. In both cases, there is no loss in the photocatalytic activity over three photocatalytic cycles, demonstrating great potential for application in energy recovery from tanning waste with simultaneous abatement of sulfide, one of the main pollutants from leather processing.

Acknowledgements The authors acknowledge the Brazilian research funding agencies Conselho Nacional de Desenvolvimento Científico e Tecnológico (CNPq, Grant Number 442840/2014-4), Fundação de Amparo à Pesquisa do Estado da Bahia (FAPESB, Grant Number APP0050/2016) and Coordenação de Aperfeiçoamento de Pessoal de Nível Superior (CAPES, Finance Code 001) for financial support. The authors are also thankful to Laboratório Multi-Usuário de Microscopia Eletrônica da UFBA (LAMUME) for Raman and SEM analyses.

Compliance with ethical standards

Conflict of interest The authors declare that they have no conflict of interest.

References

1. Doble M, Kumar A (2005) Biotreatment of industrial effluents. In: Doble M (ed) Tannery effluent, chapter 12. Butterworth-Heinemann
2. Lofrano G, Meriç S, Zengin GE, Orhon D (2013) Chemical and biological treatment technologies for leather tannery chemicals and wastewaters: a review. Sci Total Environ 461–462:265–281

3. Morera JM, Bartolí E, Gavilanes RM (2016) Hide unhairing: achieving lower pollution loads, decreased wastewater toxicity and solid waste reduction. J Clean Prod 112:3040–3047
4. Sivasubramanian S, Manohar BM, Rajaram A, Puvanakrishnan R (2008) Ecofriendly lime and sulfide free enzymatic dehairing of skins and hides using a bacterial alkaline protease. Chemosphere 70:1015–1024
5. Hannah RS, Roth SH (1991) Chronic exposure to low concentrations of hydrogen sulfide produces abnormal growth in developing cerebellar Purkinje cells. Neurosci Lett 122:225–228
6. Roth SH, Skrajny B, Reiffenstein RJ (1995) Alteration of the morphology and neurochemistry of the developing mammalian nervous system by hydrogen sulphide. Clin Exp Pharmacol Physiol 22:379–380
7. Awual MR (2017) Novel nanocomposite materials for efficient and selective mercury ions capturing from wastewater. Chem Eng J 307:456–465
8. Awual MR (2016) Assessing of lead(III) capturing from contaminated wastewater using ligand doped conjugate adsorbent. Chem Eng J 289:65–73
9. Awual MR, Alharthi NH, Hasan MM, Karim MR, Islam A, Znad H, Hossain MA, Halim ME, Rahman MM, Khaleque MA (2017) Inorganic-organic based novel nano-conjugate material for effective cobalt(II) ions capturing from wastewater. Chem Eng J 324:130–139
10. Awual MR, Hasan MM, Eldesoky GE, Khaleque MA, Rahman MM, Naushad M (2016) Facile mercury detection and removal from aqueous media involving ligand impregnated conjugate nanomaterials. Chem Eng J 290:243–251
11. Awual MR, Miyazaki Y, Taguchi T, Shiwaku H, Yaita T (2016) Encapsulation of cesium from contaminated water with highly selective facial organic–inorganic mesoporous hybrid adsorbent. Chem Eng J 291:128–137
12. Gupta R, Gupta SK, Pathak DD (2019) Selective adsorption of toxic heavy metal ions using guanine-functionalized mesoporous silica [SBA- 16-g] from aqueous solution. Microporous Mesoporous Mater. https://doi.org/10.1016/j.micromeso.2019.109577
13. Awual MR (2016) Solid phase sensitive palladium(II) ions detection and recovery using ligand based efficient conjugate nanomaterials. Chem Eng J 300:264–272
14. Awual MR (2017) New type mesoporous conjugate material for selective optical copper(II) ions monitoring & removal from polluted waters. Chem Eng J 307:85–94
15. Awual MR (2015) A novel facial composite adsorbent for enhanced copper(II) detection and removal from wastewater. Chem Eng J 266:368–375
16. Awual MR (2019) An efficient composite material for selective lead(II) monitoring and removal from wastewater. J Environ Chem Eng 7:103087
17. Awual MR (2019) A facile composite material for enhanced cadmium(II) ion capturing from wastewater. J Environ Chem Eng 7:103378
18. Awual MR (2019) Novel ligand functionalized composite material for efficient copper(II) capturing from wastewater sample. Compos B 172:387–396
19. Awual MR (2019) Mesoporous composite material for efficient lead(II) detection and removal from aqueous media. J Environ Chem Eng 7:103124
20. Lin K-YA, Lin C-H, Chen S-Y, Yang H (2016) Enhanced photocatalytic reduction of concentrated bomate in the presence of alcohols. Chem Eng J 303:596–603
21. Zhao Y, Ma L, Chang W, Huang Z, Feng X, Qi X, Li Z (2018) Efficient photocatalytic degradation of gaseous N,N-dimethylformamide in tannery waste gas using doubly open-ended Ag/TiO_2 nanotube array membranes. Appl Surf Sci 444:610–620
22. Goutam SP, Saxena G, Singh V, Yadav AK, Bharagava RN, Thapa KB (2018) Green synthesis of TiO_2 nanoparticles using leaf extract of *Jatropha curcas L.* for photocatalytic degradation of tannery wastewater. Chem Eng J 336:386–396
23. Zhao Y, Huang Z, Chang W, Wei C, Feng X, Ma L, Qi X, Li Z (2017) Microwave-assisted solvothermal synthesis of hierarchical TiO_2 microspheres for efficient electro-field-assisted-photocatalytic removal of tributyltin in tannery wastewater. Chemosphere 179:75–83
24. Vaiano V, Iervolino G (2018) Facile method to immobilize ZnO particles on glass spheres for the photocatalytic treatment of tannery wastewater. J Colloid Interface Sci 518:192–199
25. Lam S-M, Kee M-W, Sin J-C (2018) Influence of PVP surfactant on the morphology and properties of ZnO micro/nanoflowers for dye mixtures and textile wastewater degradation. Mater Chem Phys 212:35–43
26. Sivagami K, Sakthivel KP, Nambi IM (2018) Advanced oxidation processes for the treatment of tannery wastewater. J Environ Chem Eng 6:3656–3663
27. Hashem MA, Nur-A-Tomal MS, Bushra SA (2016) Oxidation-coagulation-filtration processes for the reduction of sulfide from the hair burning liming wastewater in tannery. J Clean Prod 127:339–342
28. Sengil IA, Kulaç S, Özacar M (2009) Treatment of tannery liming drum wastewater by electrocoagulation. J Hazard Mater 167:940–946
29. Suib SL (2013) New and future developments in catalysis—solar photocatalysis. Elsevier, Amsterdam
30. Preethi V, Kanmani S (2013) Photocatalytic hydrogen production. Mater Sci Semicond Proc 16:561–575
31. Puga AV (2016) Photocatalytic production of hydrogen from biomass-derived feedstocks. Coord Chem Rev 315:1–66
32. Melo MO, Silva LA (2011) Photocatalytic production of hydrogen: an innovative use for biomass derivatives. J Braz Chem Soc 22:1399–1406
33. Silva LA, Ryu SY, Choi J, Choi W, Hoffmann MR (2008) Photocatalytic hydrogen production with visible light over Pt-interlinked hybrid composites of cubic-phase and hexagonal-phase CdS. J Phys Chem C 112:12069–12073
34. Souza EA, Silva LA (2016) Energy recovery from tannery sludge wastewaters through photocatalytic hydrogen production. J Environ Chem Eng 4:2114–2120
35. Bastos SAL, Lopes PAL, Santos FN, Silva LA (2014) Experimental design as a tool to study the reaction parameters in hydrogen production from photoinduced reforming of glycerol over CdS photocatalyst. Int J Hydrogen Energy 39:14588–14595
36. Jana TK, Pal A, Chatterjee K (2014) Self assembled flower like CdS-ZnO nanocomposite and its photocatalytic activity. J Alloys Compd 583:510–515
37. Wang H, Zhang L, Chen Z, Hu J, Lu X, Li Y (2014) Semiconductor heterojunction photocatalysts: design, construction, and photocatalytic performances. Chem Soc Rev 43:5234–5244
38. Lin Y-F, Hsu Y-J (2013) Interfacial charge carrier dynamics of type-II semiconductor nanoheterostructures. Appl Catal B Environ 130–131:93–98
39. Xie YP, Yang Y, Wang G, Liu G (2017) Oxygen vacancies promoted interfacial charge carrier transfer of CdS/ZnO heterostructure for photocatalytic hydrogen generation. J Colloid Interface Sci 503:198–204
40. Tso S, Li W-S, Wu B-H, Chen L-J (2018) Enhanced H_2 production in water splitting with CdS-ZnO core-shell nanowires. Nano Energy 43:270–277
41. Velanganni S, Pravinraj S, Immanuel P, Thiruneelakandan R (2018) Nanostructure CdS/ZnO heterojunction configuration for photocatalytic degradation of Methylene blue. Physica B 534:56–62

42. Zgura I, Preda N, Socol G, Ghica C, Ghica D, Enculescu M, Frunz S (2018) Wet chemical synthesis of ZnO-CdS composites and their photocatalytic activity. Mater Res Bull 99:174–181
43. Acar C, Dincer I, Zamfirescu C (2015) A review on selected heterogeneous photocatalysts for hydrogen production. Int J Energy Res 38:1903–1920
44. Maeda K (2011) Photocatalytic water splitting using semiconductor particles: history and recent developments. J Photochem Photobiol C 12:237–268
45. Takanabe K (2017) Photocatalytic water splitting: quantitative approaches toward photocatalyst by design. ACS Catal 7:8006–8022
46. Almeida CG, Trindade TNS, Silva MVS, Silva LA (2018) Evaluation of the graphene oxide (GO) role in the photocatalytic generation of hydrogen in binary (GO-CdS) and ternary (Pt-GO-CdS) systems. Quim Nova 41:748–755
47. Mehl H, Matos CF, Neiva EGC, Domingues SH, Zarbin AJG (2014) The effect of variation of reactional parameters in the preparation of graphene by oxidation and reduction of graphite. Quim Nova 37:1639–1645
48. Compton OC, Nguyen ST (2010) Graphene oxide, highly reduced graphene oxide, and graphene: versatile building blocks for carbon-based materials. Small 6:711–723
49. Mendham J, Denney RC, Barnes JD, Thomas MJK (2000) Vogel's textbook of quantitative chemical analysis, 6th edn. Prentice-Hall, Englewood Cliffs
50. Ferreira da Silva A, Veissidi N, Na CY, Pepe I, Oliveira NB, Batista da Silva AV (1996) Optical determination of the direst bandgap energy of lead iodide crystals. Appl Phys Lett 69:1930
51. Wahab HS, Ali SH, Hussein AMA (2015) Synthesis and characterization of graphene *by Raman* spectroscopy. J Mater Sci Appl 1:130–135
52. Kumar P, Saxena N, Chandra R, Gupta V (2012) Nanotwinning and structural phase transition in CdS quantum dots. Nanoscale Res Lett 7:584
53. Zhang YC, Chen W, Hu XY (2007) Controllable synthesis and optical properties of Zn-Doped CdS nanorods from single-source molecular precursors. Cryst Growth Des 7:581–586
54. Tell B, Damen TC, Porto SPS (1966) Raman effect in cadmium sulphide. Phys Rev 144:771–774
55. Chi TTK, Gouadec G, Colomban P, Wang G, Mazerollesc L, Liemb NQ (2011) Off-resonance Raman analysis of wurtzite CdS ground to the nanoscale: structural and size-related effects. J Raman Spectrosc 42:1007–1015
56. Nikitenko VA, Plekhanov VG, Mukhin SV, Tkachev MV (1996) Raman spectra of zinc oxide powders and single crystals. J Appl Spectrosc 63:290–292
57. Ferrari AC (2007) Raman spectroscopy of graphene and graphite: disorder, electron–phonon coupling, doping and nonadiabatic effects. Solid State Commun 143:47–57
58. Dresselhaus MS, Jorio A, Filho AGS, Saito R (2010) Defect characterization in graphene and carbon nanotubes using Raman spectroscopy. Philos Trans R Soc 368:5355–5377
59. Chuang C-H, Wang Y-F, Shao Y-C, Yeh Y-C, Wang D-Y, Chen C-W, Guo JH (2014) The effect of thermal reduction on the photoluminescence and electronic structures of graphene oxides. Sci Rep 4:4525
60. Abid PS, Islam SS, Mishra Ahmad P S (2018) Reduced graphene oxide (rGO) based wideband optical sensor and the role of Temperature, Defect States and Quantum Efficiency. Sci Rep 8:3537
61. Xue C, Yan X, An H, Li H, Wei J, Yang G (2018) Bonding CdS-Sn_2S_3 eutectic clusters on graphene nanosheets with unusually photoreaction-driven structural reconfiguration effect for excellent H_2 evolution and Cr(VI) reduction. Appl Catal B Environ 222:157–166
62. Chen F, Zhang L, Wang X, Zhang R (2017) Noble-metal-free NiO@Ni-ZnO/reduced graphene oxide/CdS heterostructure for efficient photocatalytic hydrogen generation. Appl Surf Sci 422:962–969
63. Ali MB, Jo W-K, Elhouichet H, Boukherrou R (2017) Reduced graphene oxide as an efficient support for CdS-MoS_2 heterostructures for enhanced photocatalytic H_2 evolution. Int J Hydrogen Energy 42:16449–164458
64. Kumar DP, Hong S, Reddy DA, Kim TK (2017) Ultrathin MoS_2 layers anchored exfoliated reduced graphene oxide nanosheet hybrid as a highly efficient cocatalyst for CdS nanorods towards enhanced photocatalytic hydrogen production. Appl Catal B Environ 212:7–14
65. Liu S, Chen Z, Zhang N, Tang Z-R, Xu Y-J (2013) An efficient self-assembly of CdS nanowires–reduced graphene oxide nanocomposites for selective reduction of nitro organics under visible light irradiation. J Phys Chem C 117:8251–8261
66. Li X, Shen R, Ma S, Chen X, Xie J (2018) Graphene-based heterojunction photocatalysts. Appl Surf Sci 430:53–107
67. Zhou T, Chen F, Liu K, Deng H, Zhang Q, Feng J, Fu Q (2011) A simple and efficient method to prepare graphene by reduction of graphite oxide with sodium hydrosulfite. Nanotechnology 22:045704
68. Leo IM, Soto E, Vaquero F, Mota N, Fierro JLG (2017) Influence of the reduction of graphene oxide (rGO) on the structure and photoactivity of CdS-rGO hybrid systems. Int J Hydrogen Energy 42:13691–13703
69. Lei Y, Yang C, Hou J, Wang F, Min S, Ma X, Huang K-W (2017) Strongly coupled CdS/graphene quantum dots nanohybrids for highly efficient photocatalytic hydrogen evolution: unraveling the essential roles of graphene quantum dots. Appl Catal B Environ 216:59–69
70. Xu J, Wang L, Cao X (2016) Polymer supported graphene–CdS composite catalyst with enhanced photocatalytic hydrogen production from water splitting under visible light. Chem Eng J 283:816–825
71. Hong Y, Shi P, Wang P, Yao W (2015) Improved photocatalytic activity of CdS/reduced graphene oxide (RGO) for H_2 evolution by strengthening the connection between CdS and RGO sheets. Int J Hydrogen Energy 40:7045–7051
72. Singh A, Sinha ASK (2018) Active CdS/rGO photocatalyst by a high temperature gas-solid reaction for hydrogen production by splitting of water. Appl Surf Sci 430:184–197
73. Khan ME, Khan MM, Cho MH (2016) CdS-graphene nanocomposite for efficient visible-light-driven photocatalytic and photoelectrochemical applications. J Colloid Interface Sci 482:221–232